

SPITZER SPECTRAL LINE MAPPING OF PROTOSTELLAR OUTFLOWS. I. BASIC DATA AND OUTFLOW ENERGETICS

DAVID A. NEUFELD¹, BRUNELLA NISINI², TERESA GIANNINI², GARY J. MELNICK³, EDWIN A. BERGIN⁴, YUAN YUAN¹,
 SÉBASTIEN MARET⁵, VOLKER TOLLS³, ROLF GÜSTEN⁶, AND MICHAEL J. KAUFMAN⁷

¹ Department of Physics and Astronomy, Johns Hopkins University, 3400 North Charles Street, Baltimore, MD 21218, USA

² INAF—Osservatorio Astronomico di Roma, via Frascati 33, I-00040 Monte Porzio, Italy

³ Harvard-Smithsonian Center for Astrophysics, 60 Garden Street, Cambridge, MA 02138, USA

⁴ Department of Astronomy, University of Michigan, 825 Dennison Building, Ann Arbor, MI 48109, USA

⁵ Laboratoire d’Astrophysique de Grenoble, Observatoire de Grenoble, Université Joseph Fourier, CNRS, UMR 571, BP 53, F-38041 Grenoble, France

⁶ Max Planck Institut für Radioastronomie, Auf dem Hügel 69, D-53121, Bonn, Germany

⁷ Department of Physics and Astronomy, San Jose State University, One Washington Square, San Jose, CA 95192, USA

Received 2009 July 20; accepted 2009 October 7; published 2009 October 28

ABSTRACT

We report the results of spectroscopic mapping observations carried out toward protostellar outflows in the BHR71, L1157, L1448, NGC 2071, and VLA 1623 molecular regions using the Infrared Spectrograph (IRS) of the *Spitzer Space Telescope*. These observations, covering the 5.2–37 μm spectral region, provide detailed maps of the eight lowest pure rotational lines of molecular hydrogen and of the [Si I] 25.25 μm and [Fe II] 26.0 μm fine-structure lines. The molecular hydrogen lines, believed to account for a large fraction of the radiative cooling from warm molecular gas that has been heated by a non-dissociative shock, allow the energetics of the outflows to be elucidated. Within the regions mapped toward these five outflow sources, total H_2 luminosities ranging from 0.02 to 0.75 L_\odot were inferred for the sum of the eight lowest pure rotational transitions. By contrast, the much weaker [Fe II] 26.0 μm fine-structure transition traces faster, dissociative shocks; here, only a small fraction of the fast shock luminosity emerges as line radiation that can be detected with *Spitzer*/IRS.

Key words: ISM: abundances – ISM: clouds – ISM: molecules – molecular processes – shock waves

Online-only material: color figures

1. INTRODUCTION

It has long been recognized that the formation of stars in molecular clouds is often accompanied by supersonic outflows (e.g., Bally & Lada 1983). Where protostellar outflows strike nearby molecular material, and shock waves can be created; these compress and heat the gas, and can modify its composition. Interstellar shocks have been the subject of extensive study, both observational and theoretical (summarized, for example, in the review of Draine & McKee 1993). Slow shocks—propagating at speeds less than $\sim 50 \text{ km s}^{-1}$ (in clouds with typical magnetic fields)—leave the gas predominantly molecular in their wake, although the chemical composition can be modified by two processes: (1) the sputtering of dust grains and their icy mantles, which releases material into the gas phase; and (2) the enhancement of gas-phase chemical reactions that possess activation energy barriers; these may be negligibly slow at the typical temperatures of molecular clouds but rapid at the elevated temperatures behind shock waves. Faster shocks can lead to the collisional dissociation of molecules and the ionization of the resultant atoms.

The Infrared Spectrograph (IRS) of the *Spitzer Space Telescope* provides a valuable tool for observing emissions from shocked interstellar gas. With its coverage of 5.2–37 μm spectral region, IRS has provided access to (1) the lowest eight pure rotational transitions of molecular hydrogen (e.g., Neufeld et al. 2006a, hereafter N06)—the dominant constituent of molecular clouds; (2) pure rotational transitions of HD (e.g., Neufeld et al. 2006b), H_2O , and OH (e.g., Melnick et al. 2008); (3) rovibrational transitions of CO_2 and C_2H_2 (e.g., Sonnentrucker et al. 2006, 2007); and (4) fine-structure emissions of several atoms and atomic ions (Neufeld et al. 2007, hereafter N07). Observations of shocked material at mid-

infrared wavelengths offer significant advantages over ultraviolet, optical, or even near-infrared studies: they are affected less by interstellar extinction, and they can probe cooler material than can be observed at shorter wavelengths.

In this paper, we present the results of spectroscopic mapping observations carried out using the *Spitzer*/IRS toward shocked material associated with five protostellar outflows: BHR71, L1157, L1448, NGC 2071, and VLA 1623. In Section 2 below, we discuss the properties of the individual sources and the rationale underlying our source selection. In Section 3, we describe the observations, discuss our data reduction procedure, and present average spectra and spectral line maps for each source. In Section 4, we discuss the basic features of the H_2 rotational emissions and atomic fine-structure emissions that we detected; here we analyze the overall energetics for each source, describe the correlations among the various detected line emissions, and compare our H_2 spectral line maps with continuum maps obtained previously using *Spitzer*’s Infrared Array Camera (IRAC) and extracted by us from the *Spitzer* archive.

2. SOURCE SELECTION

The sample selected for the present investigation is composed of five well-studied protostellar outflows, namely, L1448, BHR71, VLA 1623, L1157 and NGC 2071, that are known to contain warm molecular gas from ground-based observations of H_2 vibrational emissions.

Our sample is not intended to provide an unbiased survey of protostellar outflows. The first four sources listed above are all outflows driven by low-mass, low-luminosity ($L < 70 L_\odot$) protostars that provide a particularly “clean” laboratory for studying shock physics. The fifth source, NGC 2071, contains a

cluster of intermediate-mass protostars with a higher luminosity ($L \sim 500 L_{\odot}$); and thus allows us to contrast the outflows associated with low-mass objects with those driven by intermediate-mass protostars. The new observations of this source complement previous *Spitzer* observations of a single $1' \times 1'$ region that have led recently to the first detection of spatially extended water (Melnick et al. 2008).

All the sources in our target list have been extensively studied at several wavelengths using a variety of different facilities; and all of them will be observed as part of the Herschel Guaranteed Time Key Program Water in Star-forming Regions with Herschel (WISH). We have provided a description of NGC 2071 in a recent paper (Melnick et al. 2008); the properties of the other four sources are reviewed below. Figures 1–5 indicate the regions mapped in each source.

2.1. BHR71

BHR 71 (also known as DC 297.2–2.8 or Sa 136) is a well-isolated Bok globule located at a distance of ~ 200 pc toward the constellation Musca (Sandqvist 1977; Bourke et al. 1995a; Bourke et al. 1995b). CO observations of this source reveal a highly collimated bipolar outflow (Bourke et al. 1997) associated with IRAS 11590–6452, which was classified as a very young Class 0 protostar with a luminosity of $\sim 9 L_{\odot}$. Higher spatial resolution observations using ISOCAM, combined with ground-based near-infrared K' -band ($2.11 \mu\text{m}$) imaging and $^{12}\text{CO } J = 2 \rightarrow 1$ observations, show that the *IRAS* source is likely composed of two embedded protostars, IRS 1 and IRS 2, with a projected separation of $\sim 17''$ (3400 AU; Bourke 2001). IRS 1 and IRS 2 each drives a molecular outflow, though the significantly larger outflow, and the one of greater interest here, is driven by IRS 1.

Recent observations of the circumstellar envelope around IRS 1 and IRS 2 by Chen et al. (2008) using both the Australian Telescope Compact Array and *Spitzer*, reveal masses of $2.12 M_{\odot}$ and $0.05 M_{\odot}$, hydrogen ($\text{H}+2\text{H}_2$) densities of 2.6×10^7 and $2.2 \times 10^7 \text{ cm}^{-3}$, and hydrogen column densities of 9.4×10^{23} and $2.6 \times 10^{23} \text{ cm}^{-2}$, respectively. Fits to the spectral energy distribution of IRS 1 and IRS 2 based on these more recent data imply bolometric luminosities for these objects of $13.5 L_{\odot}$ and $0.5 L_{\odot}$, respectively.

The *Spitzer*/IRAC image of BHR 71 is shown in Figure 1. Larger scale, multi-transition CO maps reveal that the BHR 71 outflow extends $\pm 4'$ from IRS 1. Excitation analysis implies $30 \text{ K} < T < 50 \text{ K}$ and $10^5 \text{ cm}^{-3} < n(\text{H}_2) < 3 \times 10^5 \text{ cm}^{-3}$ for the IRS 1 outflow. Though smaller, the outflow from IRS 2 appears to contain warmer gas, i.e., $T > 300 \text{ K}$ (Parise et al. 2006). The CO column densities associated with the outflow lobes from IRS 1 are estimated to be $(2-3) \times 10^{17} \text{ cm}^{-2}$. Assuming $n(\text{CO})/n(\text{H}_2) = 10^{-4}$, the inferred H_2 column density toward each lobe is $(2-3) \times 10^{21} \text{ cm}^{-2}$. Bourke et al. (1997) find the observed morphology and velocity structure of the flow are well accounted for with a simple model of a biconical outflow with a semi-opening angle of 15° , in which the gas moves outward with a constant radial velocity (with respect to the cone apex) of $\sim 28 \text{ km s}^{-1}$ and that is viewed nearly perpendicular to its symmetry axis. The inclination of the outflow axis from the line of sight is found to be $\sim 84^\circ$. The flow masses within each lobe, taking into account the mass in the velocity range of the ambient cloud and optical depth effects of the flowing gas, are 0.3 and $1.0 M_{\odot}$ for the southern and northern lobes, respectively. The mechanical luminosity of the molecular outflow, derived from $^{12}\text{CO } (1-0)$ and $^{13}\text{CO } (1-0)$ observations,

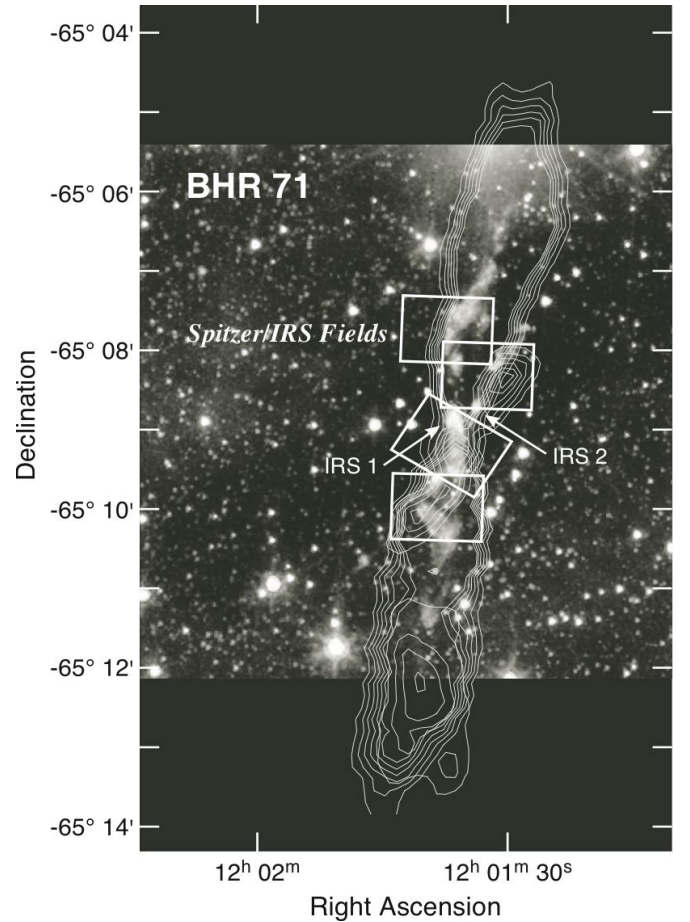


Figure 1. IRAC four-band gray-scale image of the BHR71 region on which are superposed contours of integrated CO(3–2) emission (Parise et al. 2006). The positions of the two Class 0 sources associated with BHR 71 are shown; IRS 1 is believed responsible for driving the north–south outflow, while IRS 2 is driving a much smaller east–west outflow. The rectangles denote the fields surveyed by *Spitzer*/IRS (for the LH module).

is $\sim 0.5 L_{\odot}$ and its dynamical age is $\sim 10^4$ yr (Bourke et al. 1997).

2.2. L1157

The well-collimated molecular outflow in L1157 lies deeply embedded within an extended circumstellar envelope with which it is interacting (Gueth et al. 2003; Beltrán et al. 2004). The driving source is believed to be a Class 0, low-luminosity ($11 L_{\odot}$) *IRAS* source, IRAS 20386+6751 (André et al. 1993). The outflow is approximately oriented north–south and extends over about $5'$. The distance to L1157 is assumed to share that of other clouds in Cepheus. Unfortunately, estimates for the distances of these clouds cover a fairly wide range: 200–450 pc (e.g., Kun 1998; Looney et al. 2007). Though the distance appropriate for L1157 is uncertain and remains a matter of debate, we adopt a value of 440 pc (Viotti 1969).

Figure 2 shows the *Spitzer*/IRAC image of L1157. There are notable asymmetries between the northern and the southern lobe, but the morphology is clearly S-shaped indicating the presence of an underlying precessing jet. Modeling of the outflow provides evidence for three or four separate episodes of mass ejection from the driving source over a period of $\sim 15,000$ yr (Bachiller et al. 2001). Observations of a number of excited molecular transitions clearly indicate that shocks are present in both lobes. Near-infrared $\text{H}_2 v = 1-0 \text{ S}(1) +$

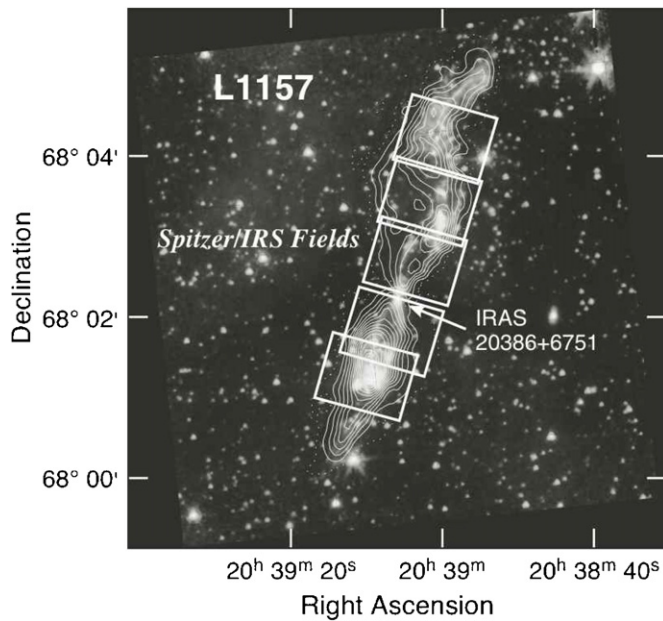


Figure 2. IRAC gray-scale image of the L1157 region. The color stretch is slightly exaggerated to emphasize channel 4 ($8\ \mu\text{m}$), where the extinction is the largest. Superposed on the *Spitzer* image is the CO (2–1) emission from Bachiller et al. (2001). The position of the driving source, IRAS 20386+6751, is shown along with the fields surveyed by *Spitzer*/IRS (LH module).

continuum imaging (Davis & Eisloffel 1995) reveal a number of knots of H_2 emission corresponding to the peaks seen in the *Spitzer*/IRAC image, with the most prominent of these H_2 emission peaks lying approximately $1'0$ to the southeast and $1'2$ to the northwest of IRAS 20386+6751. Similarly, enhanced SiO and NH_3 (3,3) emission has been detected associated with the outflow (Mikami et al. 1992; Bachiller et al. 1993), consistent with elevated temperatures and an abundance increase tied to the passage of a shock. Moreover, the spatial coincidence of the SiO and NH_3 (3,3) emission with that of the $\text{H}_2\ v = 1-0\ S(1)$ emission confirm that these emission lines arise in shocked material along the outflow.

Multi-transition CO observations of the blue-shifted southern lobe suggest that the bulk of the outflow consists of moderately dense gas of $n(\text{H}_2) = (1-3) \times 10^4\ \text{cm}^{-3}$ heated to $T_{\text{kin}} = 50-170\ \text{K}$ (Hirano & Taniguchi 2001). The intense thermal emission lines of SiO and CS preferentially sample more compact regions within the CO-defined outflow lobe with densities, $n(\text{H}_2)$, of $(1-5) \times 10^5\ \text{cm}^{-3}$ (see Mikami et al. 1992; Nisini et al. 2007). Bachiller & Pérez Gutiérrez (1997) have obtained estimates of the column density for a number of molecular species toward the driving source and two positions in the southern lobe. Using the reported column densities for ^{13}CO (1–0, 2–1) and assuming an abundance relative to H_2 of 1.1×10^{-6} , we obtain a total H_2 column density of $4.7 \times 10^{21}\ \text{cm}^{-2}$ toward the center of the outflow ($\alpha = 20^{\text{h}} 39^{\text{m}} 06^{\text{s}}.19$; $\delta = +68^\circ 02' 15''.9$, J2000) and $1.3 \times 10^{22}\ \text{cm}^{-2}$ $\Delta\alpha = 20''$, $\Delta\delta = -60''$ and $1.1 \times 10^{22}\ \text{cm}^{-2}$ $\Delta\alpha = 35''$, $\Delta\delta = -95''$ offset from the center position. The outflow mass and kinetic energy (not corrected for projection effects) derived from these CO observations are $0.36\ M_\odot$ and $1.8 \times 10^{44}\ \text{erg}$, respectively, for the southern lobe and $0.26\ M_\odot$ and $1.9 \times 10^{44}\ \text{erg}$, respectively, for the northern lobe.

2.3. L1448

In the vicinity of Lynds 1448, there are a number of molecular outflows that have been detected via a variety of observational

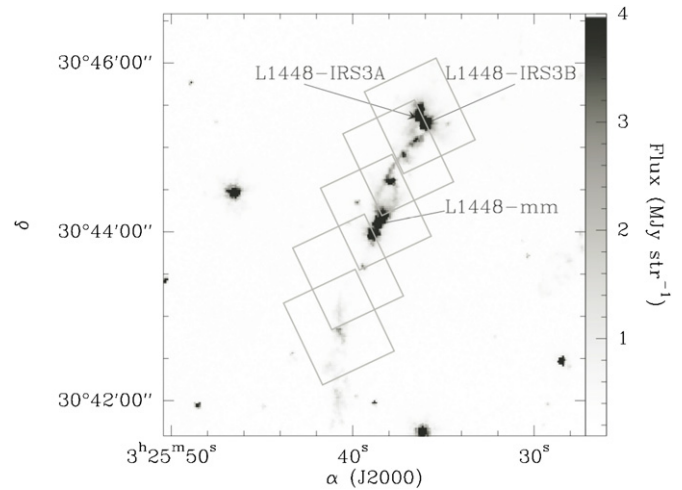


Figure 3. Image of *Spitzer*/IRAC band 2 in the region surrounding the Class 0 source L1448. Prominent sources are labeled in the image. The rectangles denote the fields surveyed by *Spitzer*/IRS (LH module).

techniques in the millimeter and infrared (e.g., Wolf-Chase et al. 2000). One of the more spectacular outflows is associated with L1448-mm (L1448C; Bachiller et al. 1991). This flow, associated with a Class 0 source, has been detected at a wide range of wavelengths and exhibits strong signatures of high-velocity gas, shock heating, and also shock chemistry. The flow was first detected in CO emission with the highest velocities ($\sim 70\ \text{km s}^{-1}$) displaying a high degree of collimation in emission morphology (Bachiller et al. 1990). The high-velocity CO gas is coincident with strong H_2 vibrational emission (Bally et al. 1993), with H_2 emission appearing illuminated on the leading edges of a bipolar cavity (Bachiller et al. 1995). The shocked gas is associated with an active chemistry with elevated abundances of SiO (Bachiller et al. 1991), CH_3OH (Jiménez-Serra et al. 2005), and H_2O (Nisini et al. 1999).

In Figure 3, we provide a finder chart illustrating our *Spitzer* IRS map coverage of the L1448-mm flow and also delineate notable sources in the region. L1448-mm or L1448C is itself a binary system, as identified in *Spitzer* images, and the flow originates in the northern source, labeled as L1448C(N) in the nomenclature of Jørgensen et al. (2006). At the tip of the northern blue-shifted lobe lies another Class 0 protostar, L1448-IRS3 (L1448-N). This source is also a binary (Looney et al. 2000) with outflow emission that corresponds to the bright spots labeled as IRS3A and 3B on the IRAC band 2 image shown in Figure 3.

Below, we provide some specifics regarding flow properties. The total mechanical luminosity of the L1448-mm flow is $\sim 1.5-3.5\ L_\odot$ (Bachiller et al. 1995; Nisini et al. 2000). The mass loss rate has some uncertainty. Nisini et al. (2000) estimate $\dot{M}_w \sim 1 \times 10^{-6}\ M_\odot\ \text{yr}^{-1}$ from far-IR cooling lines. Recent *Spitzer* data imply $\sim 10^{-6}\ M_\odot\ \text{yr}^{-1}$ and $10^{-7}\ M_\odot\ \text{yr}^{-1}$ from the atomic and molecular flows, respectively (Dionatos et al. 2009). The total $\text{H}_2\ v = 1-0\ S(1)$ luminosity from the L1448-mm flow is $\sim 0.19\ L_\odot$ (Bally et al. 1993). A comparison of the observed high- J CO, H_2O , and H_2 emission detected by Infrared Space Observatory (ISO) suggests that the flow is consistent with arising in low-velocity C-shocks ($v < 20\ \text{km s}^{-1}$; Nisini et al. 2000), but at the tip of the bow shock higher velocities ($\sim 100\ \text{km s}^{-1}$) are required (Dionatos et al. 2009). Nisini et al. (2000) estimate that $A_V \sim 6-9\ \text{mag}$ toward IRS3, $A_V \sim 4-6\ \text{mag}$ toward the tip of the L1448-mm flow, and $\sim 4.7-7\ \text{mag}$ in

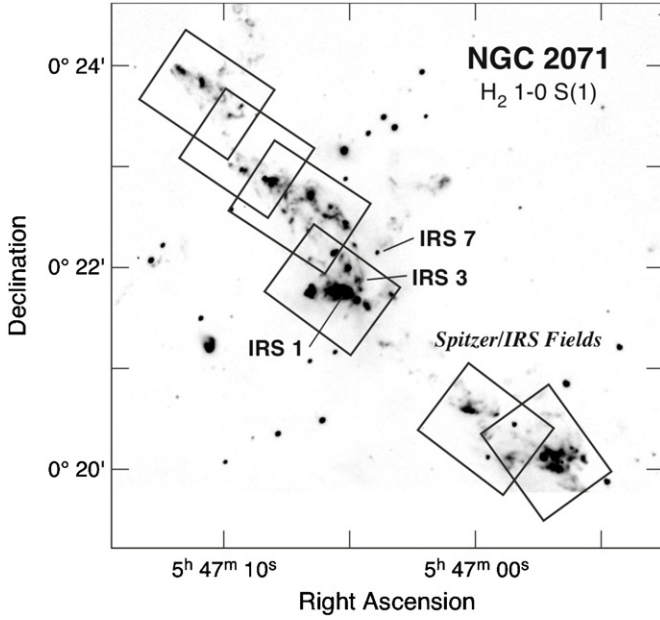


Figure 4. Map of the outflow from NGC 2071 as traced by the H_2 1–0 $S(1)$ $2.12\ \mu\text{m}$ emission (Eislöffel 2000). The rectangles denote the fields surveyed by *Spitzer*/IRS (LH module).

the southern lobe. The distance of the source is ~ 250 pc (Enoch et al. 2006).

2.4. VLA1623

The VLA1623 outflow was discovered by CO observations of cm-wave point sources coincident with ρ Oph core A (Montmerle & André 1988; André et al. 1990; Loren et al. 1990). The molecular data revealed a remarkably collimated outflow, which was notable for the clear lack of infrared point sources in the region. The detection of cold, centrally concentrated sub-mm continuum emission led this source to be known as the prototypical Class 0 source (André et al. 1993). Studies of the outflow itself find $\sim 0.1\ M_\odot$ entrained in the CO outflow (Dent et al. 1995) with an estimated wind mass loss rate of $\dot{M}_w \sim 10^{-6} M_\odot\ \text{yr}^{-1}$ and mechanical luminosity of $\sim 1.9\ L_\odot$ (Bontemps et al. 1996; André et al. 1990). The CO flow is coincident with a series of knots seen in images of H_2 vibrational emission, with a total luminosity of $L_{H_2}[1-0\ S(1)] \sim 0.04\ L_\odot$ (Dent et al. 1995; Caratti o Garatti et al. 2006).

In Figure 5, we show a finder chart showing the VLA1623 outflow as delineated by these known knots of H_2 emission. The “H” sources follow the nomenclature of Dent et al. (1995), but we also list the A (H5) and B (H4) sources as denoted by Davis & Eislöffel (1995). Additional sources in the field have been found by a deeper H_2 survey by Gómez et al. (2003). We note that source H5 is also known as HH313 and that nearby in the field is the reflection nebula associated with the Class I source GSS30 (Grasdalen et al. 1973). The rectangles show the area mapped in our *Spitzer* IRS observations, which cover the northwest red-shifted lobe of the flow encompassing from VLA1623 extending to knots H4 and H5.

Davis et al. (1999) obtained high spectral resolution observations of H_2 , S, and Q vibrational lines with a focus on knot A (HH313, H4). The resolved lines allowed an exploration of the ortho/para ratio of the hot shocked H_2 gas and they derived an ortho/para ratio of 3:1, consistent with thermal equilibrium at an estimated gas temperature in excess of 2000 K (also see

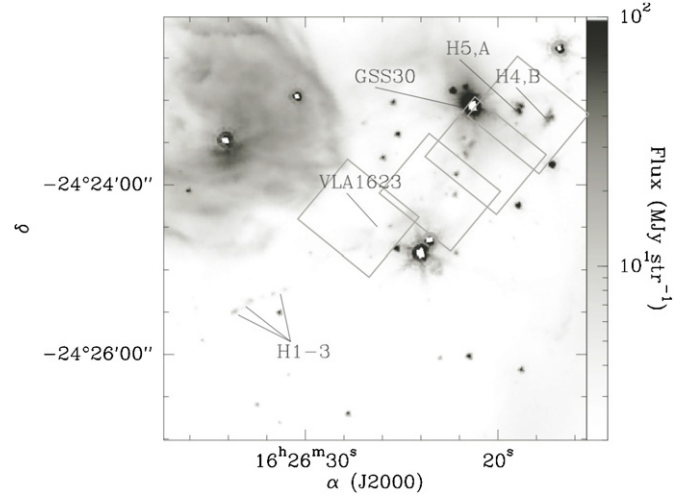


Figure 5. Image of *Spitzer*/IRAC band 2 in the region surrounding the Class 0 source VLA1623. Sources labeled with an H denote knots of vibrationally excited H_2 . Source H5 is also known as HH313. The gray boxes show the approximate coverage of our *Spitzer*/IRS maps.

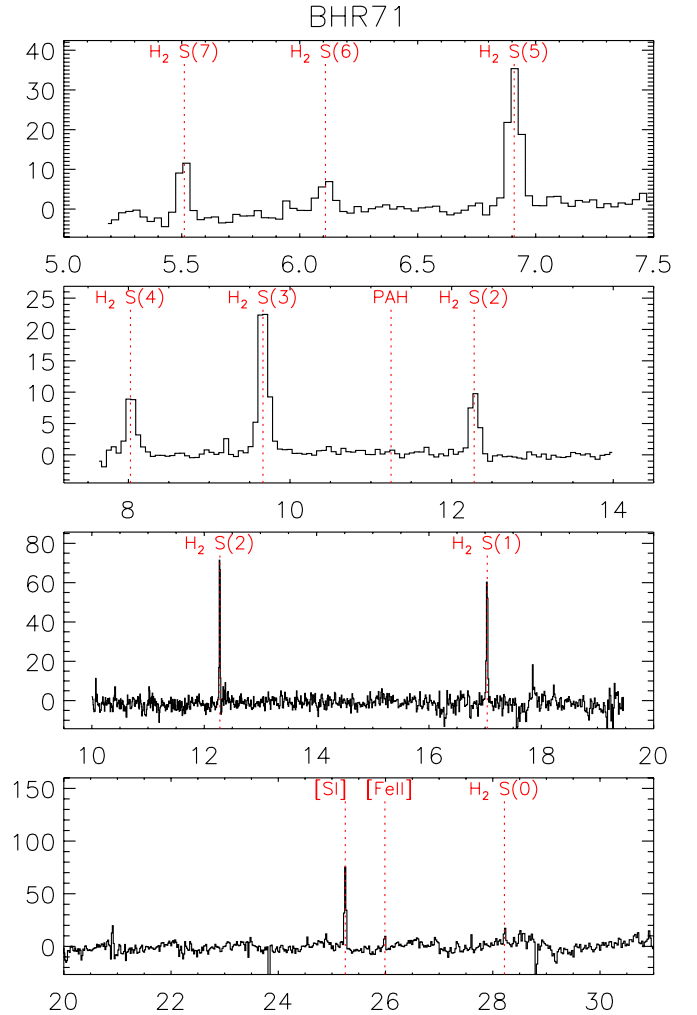


Figure 6. Example spectrum for BHR71, obtained by averaging the data over a simulated Gaussian beam of radius $25''$. The beam center position, $\alpha = 12^{\text{h}} 01^{\text{m}} 35.75^{\text{s}}$, $\delta = -65^{\circ} 07' 33''.5$ (J2000), was chosen to encompass a region of strong line emission but weak or moderate continuum emission. The wavelengths are given in units of μm , and the intensities in units of MJy sr^{-1} .

(A color version of this figure is available in the online journal.)

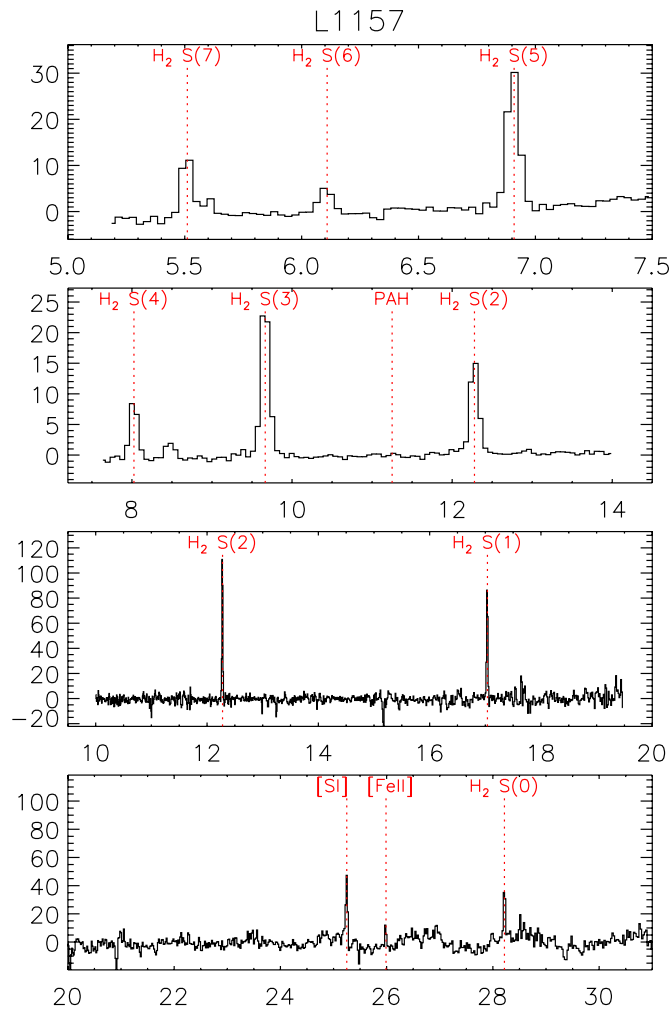


Figure 7. Same as Figure 6, but for L1157. The beam center position is $\alpha = 20^{\text{h}}39^{\text{m}}10.09^{\text{s}}$, $\delta = 68^{\circ}01'18''.9$ (J2000).

(A color version of this figure is available in the online journal.)

Eisloffel et al. 2000). In addition, through the use of line ratios between lines with similar upper state energies, they estimate a K -band extinction of $A_k = 3 \pm 1$. Recent Very Long Baseline Array (VLBA) parallax measurements of young stars associated with ρ Oph A find a distance of 120 pc (Loinard et al. 2008).

3. OBSERVATIONS AND RESULTS

The five outflow sources discussed in Section 2 above were observed with the Short-Low (SL), Short-High (SH), and Long-High (LH) modules of the IRS instrument, providing coverage of the entire 5.2–37 μm spectral region accessible to IRS at the maximum spectral resolving power available: $\lambda/\Delta\lambda \sim 60$ –127 for SL and $\lambda/\Delta\lambda \sim 600$ for SH and LH. Regions of size $\sim 1' \times 1'$ were mapped by stepping the IRS slit perpendicular to its long axis by one-half its width and, in the case of SH and LH, parallel to its long axis by 4/5 (SL) or 1/5 (LH) of its length. In each object, several such $\sim 1' \times 1'$ regions were arranged along the outflow axis to provide optimal coverage of the interaction of the outflow and the surrounding gas. In the case of the SH and LH modules, we obtained spectra of offset regions that are devoid of strong molecular emission; these were used for background subtraction. Table 1 summarizes the observational details for each object. With the exception of a

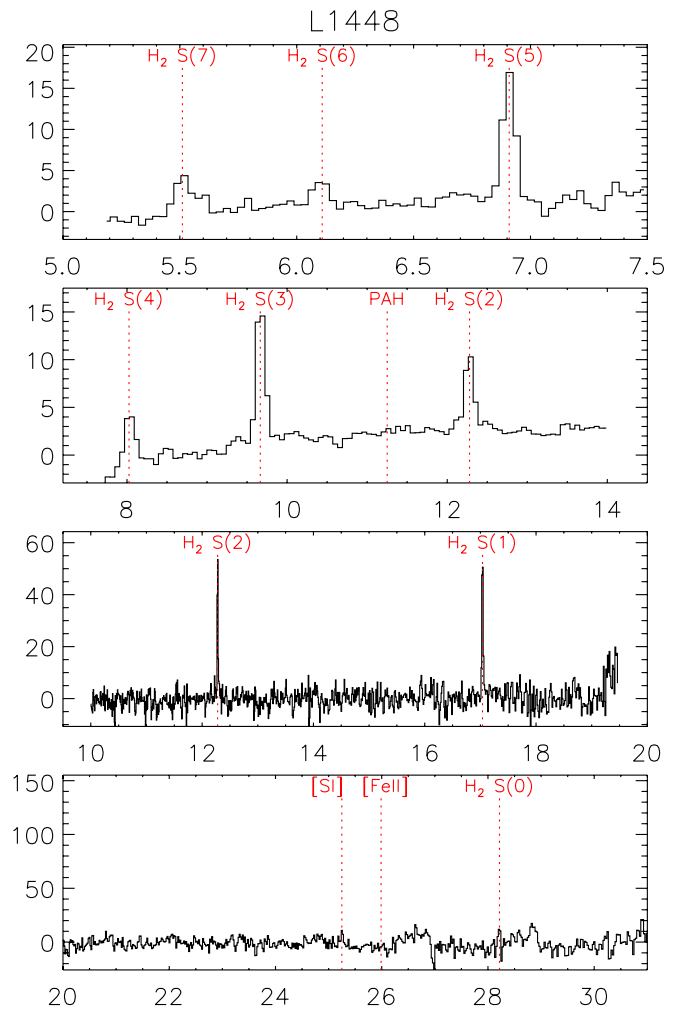


Figure 8. Same as Figure 6, but for L1448. The beam center position is $\alpha = 3^{\text{h}}25^{\text{m}}41.09^{\text{s}}$, $\delta = 30^{\circ}42'51''.8$ (J2000).

(A color version of this figure is available in the online journal.)

single $\sim 1' \times 1'$ region mapped previously toward each of BHR71 and NGC 2071, the observations were carried out in Cycle 4 of the *Spitzer* mission

The data were processed at the Spitzer Science Center, using version 17.2 or 18.0 of the processing pipeline. They were then reduced further using the SMART software package (Higdon et al. 2004), supplemented by additional routines (Neufeld et al. 2006, 2007), which provide for the removal of bad pixels in the LH and SH data, the calibration of fluxes obtained for extended sources, the extraction of individual spectra at each position sampled by the IRS slit, the creation of spectral line maps from the set of extracted spectra, the removal of striping resulting from variations in response from one pixel to another, and—in the case of the SH and LH modules—the subtraction of a background spectrum obtained at an offset position devoid of strong molecular emissions.

In Figures 6–10, we present, for each object, an example spectrum obtained by averaging the data over a simulated Gaussian beam of radius $25''$. The beam center positions, specified in Table 1, were chosen to encompass regions of strong line emission but weak or moderate continuum emission. The wavelength range plotted in Figures 6–10 is limited to 5.2–31 μm ; the quality and reliability of the spectra diminish rapidly longward of 31 μm , particularly in objects that show a strong continuum flux. In the SL modules, each example spec-

Table 1
Observational Details and Source Properties

Parameter	BHR71	L1157	L1448	NGC 2071	VLA 1623
Adopted distance (pc)	200	440	250	390	120
Map center R.A. (J2000)	12h 01m 36.07s	20h 39m 5.11s	3h 25m 38.45s	5h 47m 4.05s	16h 26m 22.96s
Map center Decl. (J2000)	−65d 08′ 50″.5	68d 02′ 43″.9	30d 44′ 13″.8	0d 21′ 56″.3	−24d 23′ 56″.2
Reference position R.A. ^a	12h 03m 40.00s	20h 38m 03.00s	3h 24m 40.00s	5h 46m 50.00s	16h 26m 11.00s
Reference position Decl. ^a	−64d 58′ 20″.0	68d 04′ 0″.0	30d 46′ 0″.0	0d 11′ 55″.0	−24d 17′ 50″.0
Start date for IRS observations	2005 Jul 02	2007 Oct 31	2008 Feb 19	2004 Oct 21	2008 Mar 27
End date for IRS observations	2008 Feb 29	2007 Nov 01	2008 Feb 29	2008 Mar 27	2008 Mar 28
IRS observing time (hr)	18.8	22.8	22.8	23.9	18.3
Beam offset ^b for plotted spectrum	(−2, 78)	(+28, −85)	(34, −82)	(63, 59)	(−53, 51)
Extinction estimate (A_V in mag)	2 ^c	2 ^c	6 ^d	13 ^e	15 ^{e,f}

Notes.

^a Used for background subtraction for the SH and LH modules.

^b ($\Delta\alpha \cos \delta$, $\Delta\delta$) relative to the map center in units of arcsec.

^c Caratti o Garatti et al. (2006).

^d Nisini et al. (2000).

^e Melnick et al. (2008).

^f Davis et al. (1999).

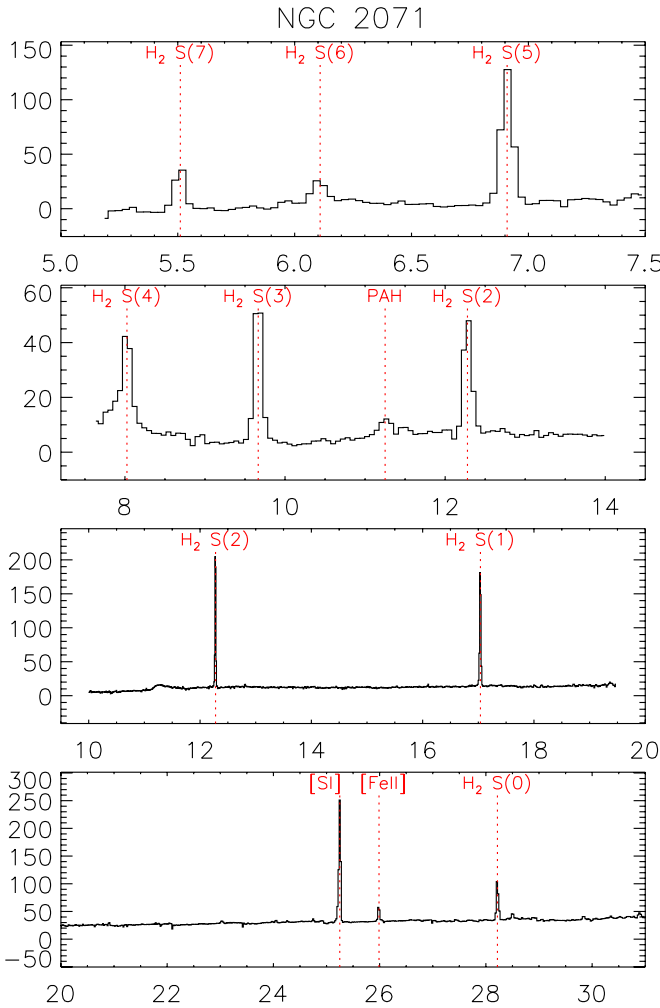


Figure 9. Same as Figure 6, but for NGC 2071. The beam center position is $\alpha = 5^{\text{h}} 47^{\text{m}} 8.25^{\text{s}}$, $\delta = 0^{\circ} 22' 55''.3$ (J2000). The weak features at $28.50 \mu\text{m}$ and $29.84 \mu\text{m}$ are the HD R(3) and $\text{H}_2\text{O } 7_{25} - 6_{16}$ transitions (discussed previously by Melnick et al. 2008).

(A color version of this figure is available in the online journal.)

trum shows a clear detection of the $\text{H}_2 \text{ S}(2)\text{--S}(7)$ pure rotational lines; in the SH module, $\text{H}_2 \text{ S}(1)$ and $\text{S}(2)$ are invariably observed with large line-to-continuum and signal-to-noise ratios;

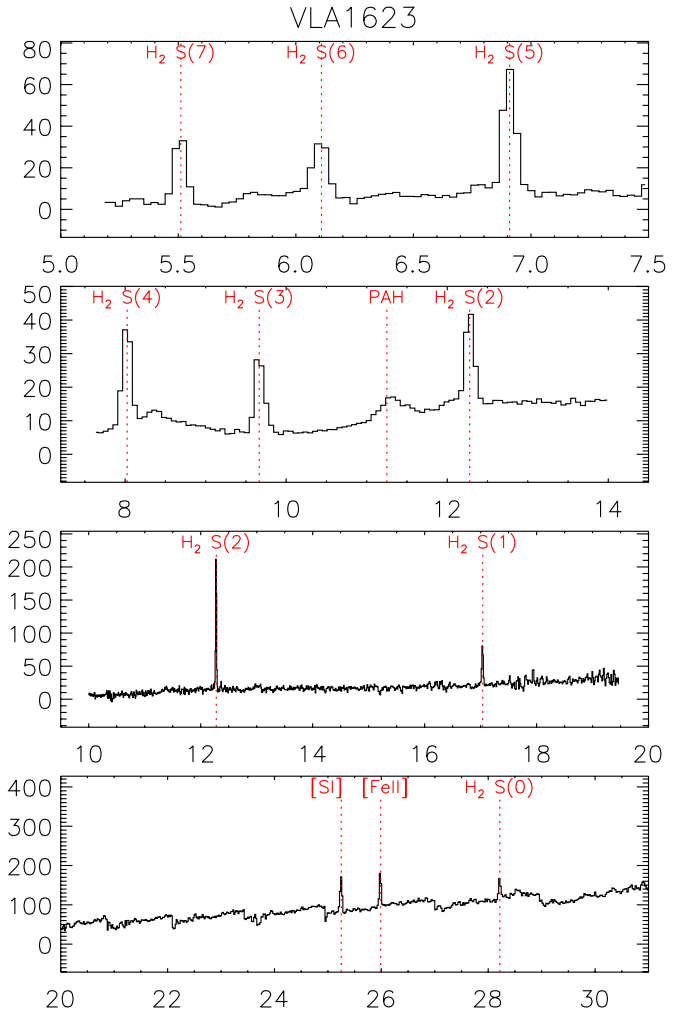


Figure 10. Same as Figure 6, but for VLA1623. The beam center position is $\alpha = 16^{\text{h}} 26^{\text{m}} 19.08^{\text{s}}$, $\delta = -24^{\circ} 24' 47''.2$ (J2000). Order mismatches are evident in the LH spectrum (bottom panel).

(A color version of this figure is available in the online journal.)

while in the LH module, $\text{H}_2 \text{ S}(0)$ is typically detected, along with the $^3\text{P}_1\text{--}^3\text{P}_2$ $25.25 \mu\text{m}$ fine-structure transition of atomic sulphur and the $^6\text{D}_{7/2}\text{--}^6\text{D}_{9/2}$ transition of singly ionized iron.

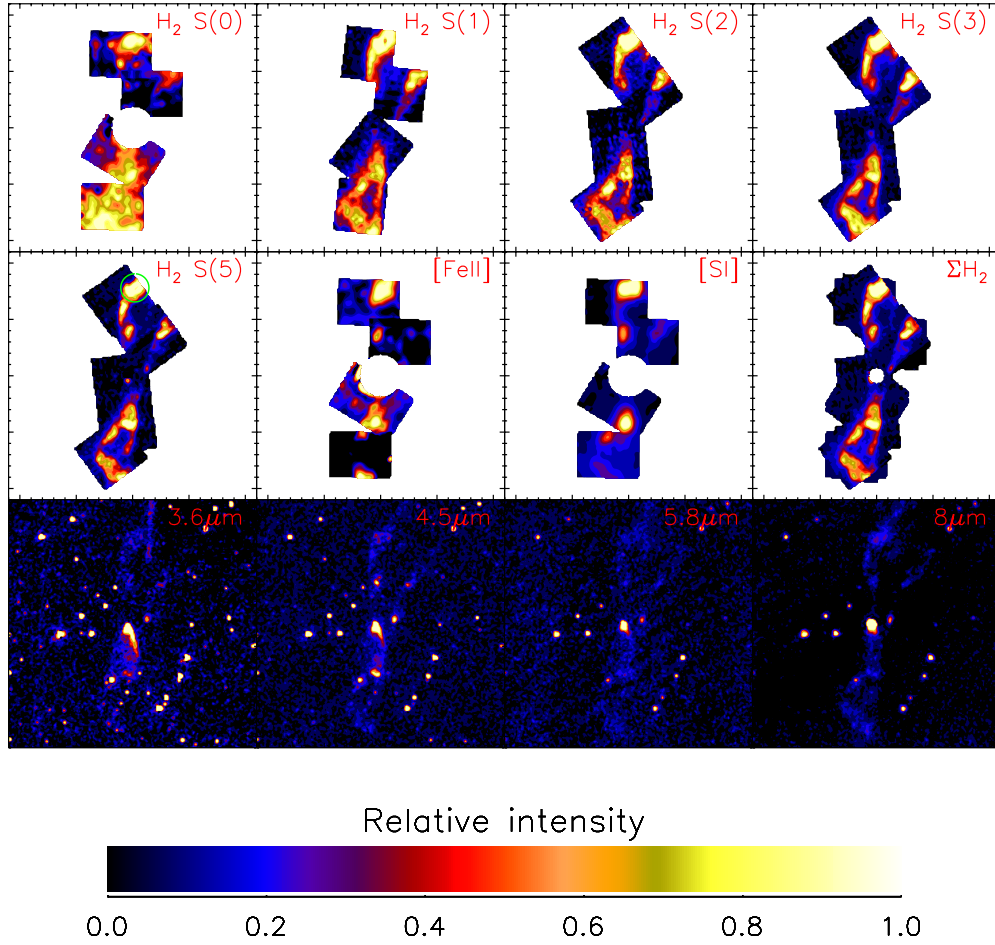


Figure 11. Spectral line maps obtained toward BHR71 for the H_2 $S(0)$, H_2 $S(1)$, H_2 $S(2)$, H_2 $S(3)$, H_2 $S(5)$, $[\text{Fe II}]$ 25.99 μm and $[\text{Si I}]$ 25.25 μm lines, together with the sum of the H_2 $S(0)$ – $S(7)$ emission lines and the archival 3.6 μm , 4.5 μm , 5.8 μm , and 8 μm IRAC maps. Each map is normalized relative to the reference intensities listed in Table 2. The map center position is $\alpha = 12^{\text{h}} 01^{\text{m}} 36.07^{\text{s}}$, $\delta = -65^{\circ} 08' 50''.5$ (J2000), and each small tick interval is 10 arcsec. The green circle indicates the size and position of the 25 arcsec diameter region for which the example spectrum was obtained. The offset of this position relative to the line center is given in Table 1.

(A color version of this figure is available in the online journal.)

Table 2
Reference Intensities for Each Map^a

Spectral Line or IRAC Band	BHR71	L1157	L1448	NGC 2071	VLA 1623
H_2 $S(5)$ 6.910 μm	372.1	262.0	256.8	1290.0	409.3
H_2 $S(3)$ 9.665 μm	239.6	256.3	225.7	628.3	183.5
H_2 $S(2)$ 12.279 μm	53.4	96.7	60.8	300.3	133.8
H_2 $S(1)$ 17.035 μm	34.5	55.0	49.4	164.2	34.1
H_2 $S(0)$ 28.219 μm	4.1	8.0	6.0	31.8	15.7
H_2 $S(0)$ – $S(7)$ total	1225.0	984.0	921.8	3912.0	1377.0
$\text{Fe}^+ \text{ } ^6D_{7/2}$ – $^6D_{9/2}$ 25.988 μm	4.5	6.1	20.5	18.7	27.0
$\text{S } ^3P_1$ – 3P_2 25.249 μm	25.0	12.3	17.0	59.5	27.3
IRAC Band 1 (3.6 μm cont.)	10	3	5	40	100
IRAC Band 2 (4.5 μm cont.)	20	3	10	100	100
IRAC Band 3 (5.8 μm cont.)	40	10	10	200	300
IRAC Band 4 (8.0 μm cont.)	20	5	10	200	500

Note.

^a In units of $10^{-6} \text{ erg cm}^{-2} \text{ s}^{-1} \text{ sr}^{-1}$ for lines and MJy sr^{-1} for continuum. The errors in the line intensities are likely dominated by systematic effects and are expected to be $\leq 25\%$ (N06).

Spectral line maps are shown in Figures 11–15. The effective angular resolution varies from $\sim 3''$ (half-power beamwidth, HPBW) for the SL module to $\sim 10''$ for the LH module (see Table 5 of N06). For each object, we present maps of the H_2 $S(0)$, H_2 $S(1)$, H_2 $S(2)$, H_2 $S(3)$, H_2 $S(5)$, $[\text{Fe II}]$ 25.99 μm , and

$[\text{Si I}]$ 25.25 μm lines, together with the sum of the H_2 $S(0)$ – $S(7)$ emission lines and the archival 3.6 μm , 4.5 μm , 5.8 μm , and 8 μm IRAC maps. The H_2 $S(4)$, $S(6)$, and $S(7)$ line maps—although somewhat noisier and not shown in Figures 11–15—all exhibit a morphology nearly identical to those of the H_2

Table 3
Measured Line Luminosities and Derived Parameters

Parameter	BHR71	L1157	L1448	NGC 2071	VLA 1623
Line luminosities ^a					
H ₂ S(7) 5.511 μm	7.1	15.3	5.0	94.5	2.1
H ₂ S(6) 6.100 μm	3.9	8.5	3.4	54.4	2.1
H ₂ S(5) 6.910 μm	11.4	27.9	9.2	206.4	5.6
H ₂ S(4) 8.025 μm	6.8	25.9	7.9	98.7	2.5
H ₂ S(3) 9.665 μm	10.1	42.1	10.8	145.7	2.7
H ₂ S(2) ^b 12.279 μm	2.2	16.2	2.9	79.0	1.6
H ₂ S(1) 17.035 μm	1.7	13.0	3.7	58.2	0.6
H ₂ S(0) 28.219 μm	0.3	2.3	0.6	12.0	0.4
H ₂ S(0)–S(7) total	43.7	151.2	43.6	748.8	17.7
Fe ⁺ ⁶ D _{7/2} – ⁶ D _{9/2} 25.988 μm	0.5	0.2	0.7	2.9	0.3
S ³ P ₁ – ³ P ₂ 25.249 μm	0.7	1.4	0.8	8.8	0.3
Contribution of H ₂ to IRAC bands (percentage)					
Band 3 (5.8 μm)	33	39	15	9.1	6.5
Band 4 (8.0 μm)	120 ^c	106 ^c	18	5.7	2.6
H ₂ excitation: best-fit parameters ^d					
H ₂ mass above 100 K ($10^{-3} M_{\odot}$)	2.5	49	8.1	177	1.3
Power law index, $b = -d\ln M/d\ln T$	2.5 ± 0.5	3.3 ± 0.5	2.9 ± 0.5	3.2 ± 0.6	$2.3^{+1.3}_{-0.8}$
$\log(\text{H}_2 \text{ density}/\text{cm}^{-3})$	3.8 ± 0.4	3.8 ± 0.5	3.8 ± 0.4	3.8 ± 0.4	$3.5^{+0.7}_{-0.1}$
Initial H ₂ OPR (OPR ₀)	≤ 2.4	≤ 1.8	Note ^e	≤ 1.8	≤ 1.9

Notes.

^a In units of $10^{-3} L_{\odot}$ for assumed distances of 200, 440, 250, 390, and 120 pc, respectively, for BHR71, L1157, L1448, NGC 2071, and VLA 1623. These values do not include any extinction correction. The errors in the line intensities are likely dominated by systematic effects and are expected to be $\leq 25\%$ (N06).

^b The luminosity for H₂ S(2) is determined from the SL module.

^c Here, the computed contribution to the 8 μm band actually exceeds 100%, a discrepancy that presumably reflects flux calibration errors that are within expectations.

^d \pm and \leq symbols indicate 95% confidence intervals.

^e No useful constraint (consistent with 3 or any smaller value).

S(3) and S(5) maps. In the present paper, we consider only those spectral lines that can be mapped reliably over most of the region sampled by our observations. Additional lines of H₂O, OH, and HD—typically much weaker than those considered here—have been detected in parts of some of our target objects (e.g., Melnick et al. 2008), and will be discussed further in upcoming papers.

Each map is normalized relative to the reference intensities listed in Table 2. For the spectral line maps, these reference intensities are not the maximum intensities but instead the values that are exceeded in only 0.1% of the mapped area;⁸ they are therefore somewhat smaller than the maximum measured intensities. For the continuum maps, the reference intensities were chosen to bring out the low-intensity regions within the maps; they are often much smaller than the maximum intensities. In the spectral line maps of BHR71, a 25'' region near the map center has been excised from observations with the LH module; here, the continuum intensity is too great to permit a reliable determination of the intensities of lines observed with the LH module. For each object, the map center is listed in Table 1, and the tick marks indicate offsets relative to that position, small tick marks being separated by 10'' and large tick marks by 50''. North is up and east is to the left. The green circle plotted on the H₂ S(5) map indicates the simulated Gaussian beam for which the example spectra in Figures 6–10 were obtained.

By integrating the line intensities over the entire mapped region for each object—but excluding the excised region in

BHR71 for those lines detected with the LH module—we obtained the total line luminosities listed in Table 3. These assume the distance estimates discussed in Section 2 and tabulated in Table 1, and assume the line emission to be isotropic, as expected for optically thin lines.

4. DISCUSSION

4.1. H₂ Rotational Emissions

The pure rotational transitions of H₂ are optically thin, and thus the level populations are readily calculable. Our observations of the S(0)–S(7) rotational emissions provide estimates of the $J = 2$ through $J = 9$ column densities. In this paper, we consider only the total H₂ luminosities for the entire mapped region in each object. We defer a detailed discussion of spatial variations in the line luminosities and line ratios to a future paper (B. Nisini et al. 2009, in preparation), in which we will also discuss existing spectral line maps of H₂ vibrational emissions. In Figure 16, we present rotational diagrams based upon the H₂ luminosities given in Table 3, corrected for extinction using the extinction estimates given in Table 1. Here, we plot the logarithm of the total number of molecules in each state, divided by the degeneracy of that state, as a function of the energy. Diamonds indicate the observed values, and the solid lines are results obtained from the fitting procedure described below. While material in thermal equilibrium at a single temperature would exhibit a linear behavior in such a plot, the observed rotational diagrams—like those obtained for outflow sources by N06 and by Maret et al.

⁸ This choice of color scale allows the lower intensity emission to be discerned more readily.

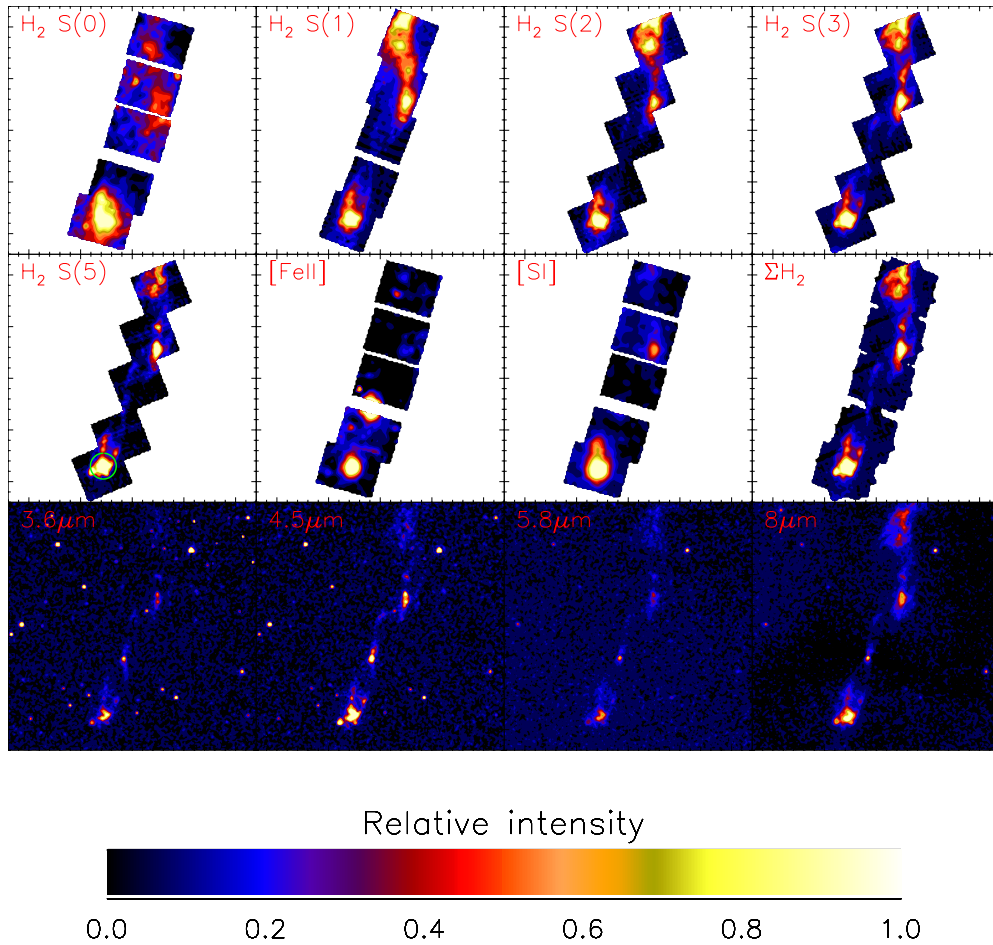


Figure 12. Same as Figure 11, but for L1157. The map center position is $\alpha = 20^{\text{h}}39^{\text{m}}5.11^{\text{s}}$, $\delta = 68^{\circ}02'43''.9$ (J2000).
(A color version of this figure is available in the online journal.)

(2009), and for supernova remnants (SNRs) by N07—depart from that behavior in two respects. First, there is a positive curvature to the rotational diagram, indicative of the presence of multiple temperature components. Second, except toward L1448, there is a characteristic zigzag behavior, most notably for the states of lowest energy, in which the states of even rotational quantum number J lie systematically above those of odd J . As in N06, N07, and Maret et al. (2009), we attribute this second behavior to an ortho-to-para ratio—smaller than the equilibrium value of 3—that is the relic of an earlier period when the gas was considerably cooler than it is now.

We have modeled the H_2 rotational diagrams in Figure 16, using a method similar to that described by Neufeld and Yuan (2008, hereafter NY08). As in NY08 (their Equation (3)), we assume a power-law distribution of gas temperatures with the number of molecules at temperature between T and $T + dT$ assumed proportional to T^{-b} . We assume a temperature range extending from $T_{\min} = 100 \text{ K}$ ⁹ to $T_{\max} = 4000 \text{ K}$. Solving the equations of statistical equilibrium for the H_2 level populations, and adopting the molecular data cited in NY08, we obtained predictions for the pure rotational line luminosities as a function of the power-law index, b , the total mass of hydrogen molecules

warmer than T_{\min} , $M_{\text{H}_2} (\geq T_{\min})$, and the H_2 density, $n(\text{H}_2)$. The excitation of pure rotational emissions is dominated by collisions with H_2 (see NY08), in contrast to the case of rovibrational emissions, where excitation by atomic hydrogen presents an additional complication that we will discuss in a future paper (B. Nisini et al. 2009, in preparation).

We have extended the treatment of NY08 by considering the H_2 ortho-to-para ratio (OPR) along with b , $M_{\text{H}_2} (\geq T_{\min})$ and $n(\text{H}_2)$. Here, we introduce two additional parameters: the initial ortho-to-para ratio, OPR_0 , and the time period, τ , for which the gas temperature has been elevated. If reactive collisions with atomic hydrogen are the dominant mechanism for the interconversion of ortho- and para- H_2 , then the ortho-to-para ratio after time τ is given by N06:¹⁰

$$\frac{\text{OPR}(\tau)}{1 + \text{OPR}(\tau)} = \frac{\text{OPR}_0}{1 + \text{OPR}_0} e^{-n(\text{H}) \tau [k_{\text{PO}} + k_{\text{OP}}]} + \frac{\text{OPR}_{\text{LTE}}}{1 + \text{OPR}_{\text{LTE}}} \times (1 - e^{-n(\text{H}) \tau [k_{\text{PO}} + k_{\text{OP}}]}), \quad (1)$$

where $n(\text{H})$ is the atomic hydrogen density, k_{PO} is the rate coefficient for para-to-ortho conversion, estimated as $8 \times 10^{-11} \exp(-3900/T) \text{ cm}^3 \text{ s}^{-1}$ by Schofield (1967), based upon the laboratory experiments of Schulz & Le Roy (1965), and $k_{\text{OP}} \sim k_{\text{PO}}/3$ is the rate coefficient for ortho-to-para conversion.

⁹ Recognizing that gas in the 100–300 K range can contribute significantly to the pure rotational line emission that we detect with *Spitzer*, we have reduced T_{\min} from 300 K in NY08 to 100 K in the present work.

¹⁰ Note that the expression given by N06 erroneously omits k_{OP} from the term $[k_{\text{PO}} + k_{\text{OP}}]$, resulting in a 25% error.

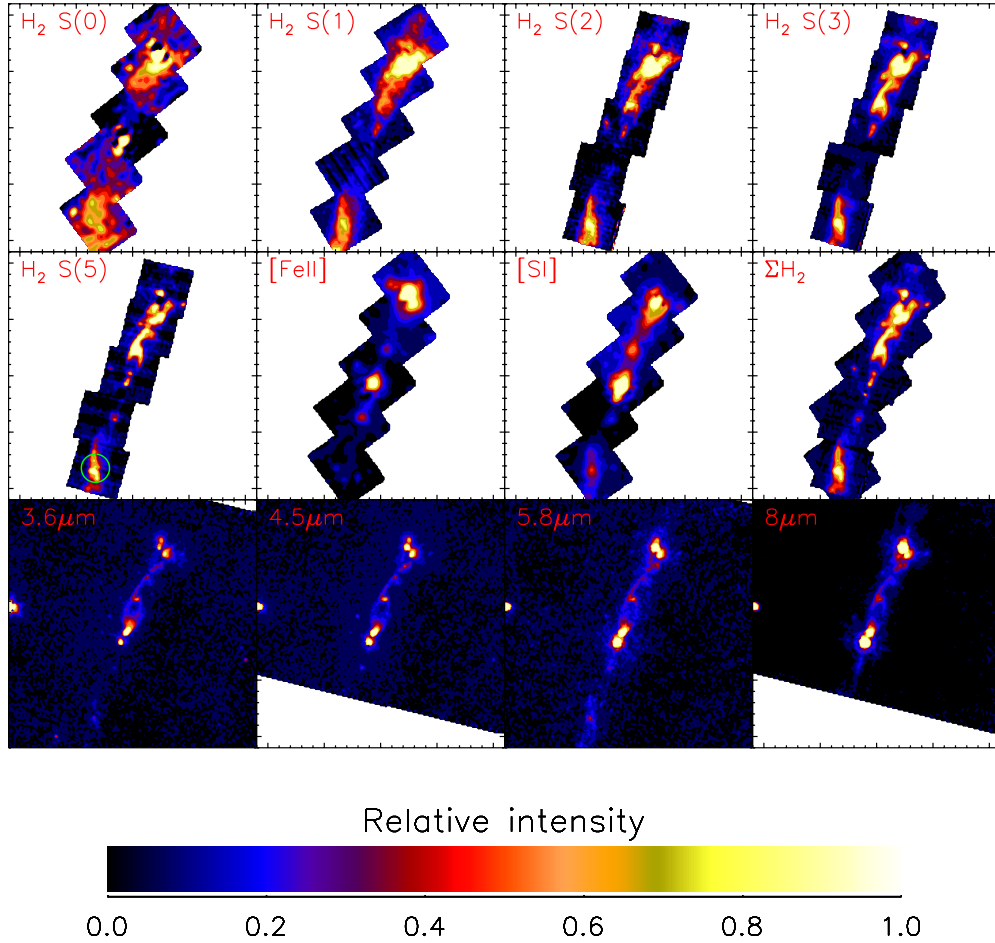


Figure 13. Same as Figure 11, but for L1448. The map center position is $\alpha = 3^{\text{h}} 25^{\text{m}} 38.45^{\text{s}}$, $\delta = 30^{\circ} 44' 13''.8$ (J2000).
(A color version of this figure is available in the online journal.)

Thanks to the strong dependence of k_{PO} upon the gas temperature, the ortho-to-para ratio is similarly temperature dependent, the warmer gas components being closer to equilibrium than the cooler ones. This effect is evident in Figure 16, the degree of zigzag being least for the highest energy states that are excited primarily in the warmest gas.

We have adjusted the five parameters b , $M(\text{H}_2)$, $n(\text{H}_2)$, OPR_0 , and $n(\text{H})\tau$ in order to obtain the best fit to the data. Here, we minimize the χ^2 for the $S(1)$ through $S(7)$ rotational lines, assuming the same fractional uncertainty for each data point. We exclude the $\text{H}_2 S(0)$ line flux from the analysis, because its value is rather uncertain, particularly in regions of strong continuum intensity where the line-to-continuum ratio becomes small. The best-fit parameters are given in Table 3.

The inferred masses of warm¹¹ H_2 (i.e., at $T \geq 100$ K) range from $1.3 \times 10^{-3} M_{\odot}$ in VLA 1623 to $0.18 M_{\odot}$ in NGC 2071. These values exclude the mass contribution from helium and apply only to the regions mapped by IRS. The best-fit power-law indices, b , range from 2.2 to 3.3. These values lie somewhat below the typical values determined by NY08 in the SNR IC443C, and somewhat below the value $b = 3.8$ expected for a paraboloidal bow shock that is dissociative at its apex. The

best-fit H_2 densities range from 3000 to 7000 cm^{-3} . It should be noted, however, that the range of acceptable values for b and $n(\text{H}_2)$ can be large, and that these two parameters are somewhat degenerate in the following sense: increasing b tends to decrease the predicted relative strength for the higher J transitions, while decreasing $n(\text{H}_2)$ has a similar effect (because the level populations become increasingly subthermal). Thus, an increase in one of these assumed parameters can partially compensate for a decrease in the other. The correlated uncertainties in b and $n(\text{H}_2)$ are presented graphically in Figure 17, which shows contours of χ^2 in the b - $n(\text{H}_2)$ plane. Crosses indicate the minimum χ^2 (i.e., the best fit), while the two contours represent the 68% and 95% confidence limits on each parameter. With the exception of L1448, for which the data are consistent with an OPR of 3, the objects require an initial OPR less than 3. In two objects, L1157 and NGC 2071, the current OPR is clearly larger for the higher J states than for the lower J states. In the context of our model for the evolution of the OPR (Equation (1)), both cases imply a lower limit $\sim 10^3 (\text{cm}^{-3}/n(\text{H})) \text{ yr}$ on the time period, τ , for which the gas has been warm.

4.2. Fine-structure Emissions

The $\text{Fe}^+ \text{}^6\text{D}_{7/2} - \text{}^6\text{D}_{9/2}$ $25.988 \mu\text{m}$ and $\text{S } ^3\text{P}_1 - ^3\text{P}_2$ $25.249 \mu\text{m}$ fine-structure lines are readily detectable in the LH spectra of all five outflow sources, and are strong enough to map. However, these transitions make a negligible contribution to the total 5.2–

¹¹ In this paper, we use the word “warm” to describe H_2 at temperatures ≥ 100 K. This, of course, includes gas at lower temperatures than that which can be probed by means of traditional, ground-based studies of vibrationally excited H_2 .

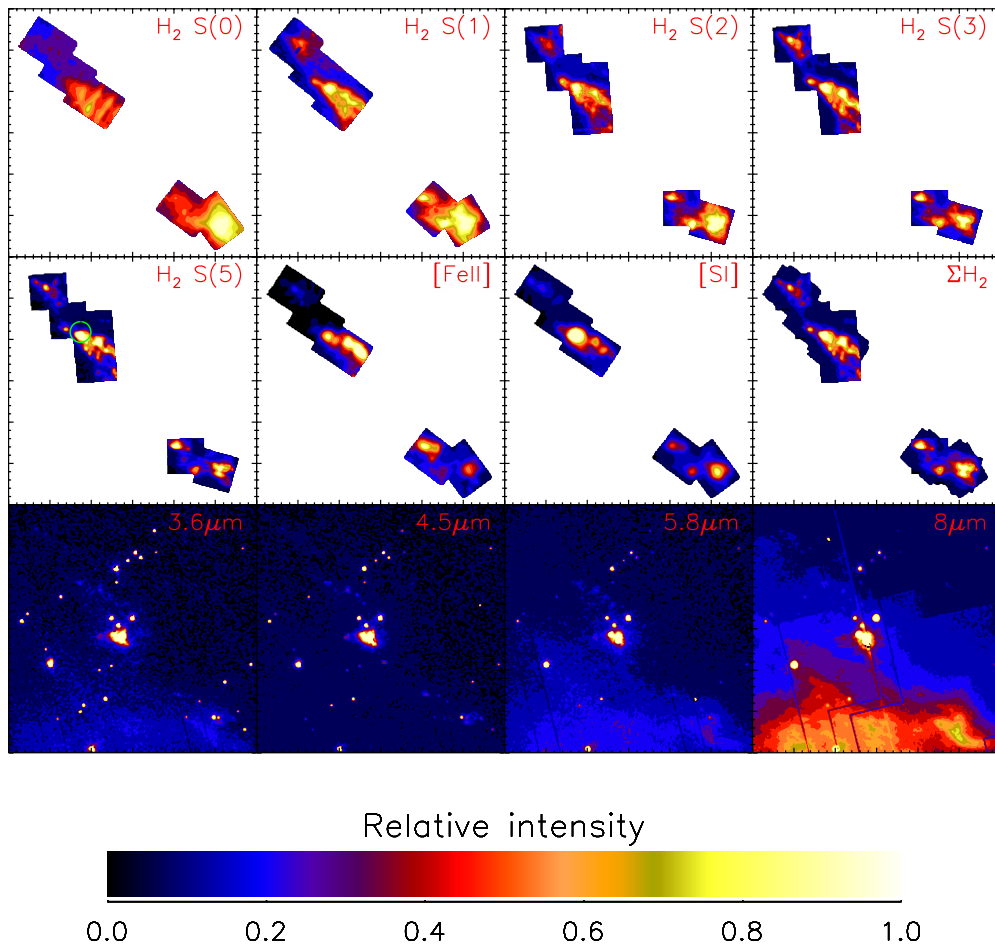


Figure 14. Same as Figure 11, but for NGC 2071. The map center position is $\alpha = 5^{\text{h}} 47^{\text{m}} 4.05^{\text{s}}$, $\delta = 0^{\circ} 21' 56''.3$ (J2000).
(A color version of this figure is available in the online journal.)

$37\ \mu\text{m}$ line luminosity. The [S I] line luminosity ranges from $\sim 1\%$ to 2% of the total H_2 $S(0)$ – $S(7)$ luminosity. For [Fe II], the corresponding range is $\sim 0.15\%$ to 2% wider. In the case of [Fe II], these percentages are much smaller than those attained in some of the SNRs that we observed previously (N07). In the SNR 3C391, for example, the [Fe II] $25.988\ \mu\text{m}$ line flux exceeded 10% of the total H_2 $S(0)$ – $S(7)$ flux. Furthermore, fine-structure emissions from more highly ionized species— Ne^+ , Ne^{++} , and S^{++} for example—are readily detectable in SNRs but not in protostellar outflow sources. These differences suggest that higher velocity shocks are more prevalent in SNRs than around outflow sources.

A visual inspection of Figures 11–15 suggests that the [S I] emissions are typically more closely correlated with the H_2 emissions than are the [Fe II] emissions. This impression is borne out by a correlation analysis. Comparing the H_2 $S(5)$ and [S I] intensities, spatial pixel by spatial pixel, we obtained linear correlation coefficients of 0.81, 0.78, 0.42, 0.80, and 0.85, respectively, for BHR71, L1157, L1448, NGC 2071, and VLA 1623. Comparing the H_2 $S(5)$ and [Fe II] intensities, the corresponding results are invariably smaller: 0.55, 0.48, 0.23, 0.72, and 0.78. This behavior is consistent with our previous study of SNRs, in which a principal component analysis suggested that the [S I] emitting region was largely cospatial with the H_2 emitting region, while emissions from ionized species such as Fe^+ originated in a separate gas component. This segregation is presumably a consequence of the different shock

velocities needed to generate [S I], H_2 , and [Fe II] emissions. The first two arise in slow non-dissociative shocks that create very little ionization, while the third arises in faster shocks that are dissociative and ionizing. According to theoretical models (e.g., Allen et al. 2008), the emission from dissociative shocks is dominated by optical and ultraviolet line emissions, with infrared fine-structure emissions accounting for only a small fraction of the overall shock luminosity.

4.3. Source Energetics and Comparison with IRAC Maps

The wavelength coverage of *Spitzer* is well suited to observing the radiative cooling of non-dissociative molecular shocks. The study of Kaufman and Neufeld (1996) indicates that over a wide range of shock parameters, pure rotational emissions from H_2 are key coolants of non-dissociative shocks. For shocks of velocity in the range 20 – $40\ \text{km s}^{-1}$ and with a preshock H_2 density of $10^4\ \text{cm}^{-3}$, for example, between 45% and 69% of the shock luminosity is predicted to emerge in pure rotational emission from H_2 . Moreover, almost all of the H_2 pure rotational emission emerges in the $S(0)$ – $S(7)$ lines accessible to *Spitzer*. The total H_2 $S(0)$ – $S(7)$ luminosities listed in Table 1 range from $0.02\ L_{\odot}$ to $0.75\ L_{\odot}$. Taking these luminosities as lower limits for the total mechanical luminosity dissipated in the shocks, adopting $20\ \text{km s}^{-1}$ as a typical shock velocity, v_s , and setting the mechanical luminosity equal to $\frac{1}{2}\dot{M}v_s^2$, we obtain lower limits on the mass flow rates through the shock, \dot{M} , ranging from $\sim 10^{-6}$ to $\sim 2 \times 10^{-5}\ M_{\odot}\ \text{yr}^{-1}$.

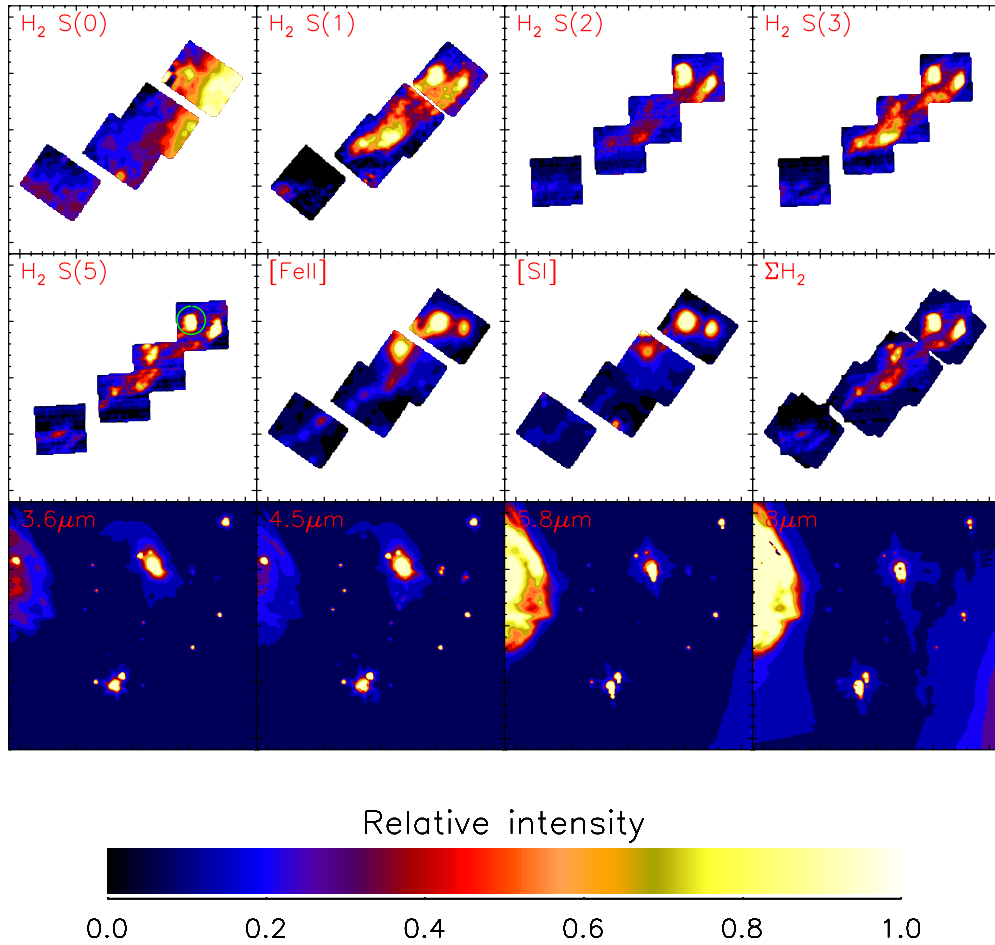


Figure 15. Same as Figure 11, but for VLA1623. The map center position is $\alpha = 16^{\text{h}} 26^{\text{m}} 22.96^{\text{s}}$, $\delta = -24^{\circ} 23' 56''.2$ (J2000).
(A color version of this figure is available in the online journal.)

In some objects, H_2 line emissions can contribute significantly to the intensities measured using broadband mid-IR photometry (e.g., Reach et al. 2006; NY08). For the SNR IC443, NY08 found that the mid-IR spectral region covered by IRAC was dominated by H_2 line emissions. In particular, the intensities measured in the $5.8 \mu\text{m}$ and $8 \mu\text{m}$ IRAC channels (Bands 3 and 4), were accounted for almost entirely by the IRS-measured H_2 $S(4)$ – $S(7)$ line intensities. Given an excitation model for H_2 , the $3.6 \mu\text{m}$ and $4.5 \mu\text{m}$ IRAC intensities could similarly be explained as resulting from H_2 emissions, primarily the $S(9)$ pure rotational emission for the $4.5 \mu\text{m}$ band and the $v = 1$ – 0 $Q(5)$ rovibrational line for the $3.6 \mu\text{m}$ band.

For the protostellar outflow sources studied here, we can evaluate the contribution of the H_2 $S(4)$ – $S(7)$ emissions to the broadband intensities measured with IRAC. In Table 3, we list the fraction of the intensities measured in the $5.8 \mu\text{m}$ and $8 \mu\text{m}$ IRAC bands that is attributable to H_2 $S(4)$ and $S(5)$ (in the case of the $8 \mu\text{m}$ band) or H_2 $S(6)$ and $S(7)$ (in the case of the $5.8 \mu\text{m}$ band). The contribution is clearly largest in BHR71 and L1157, for which the computed contribution to the $8 \mu\text{m}$ band actually exceeds 100%, a discrepancy that presumably reflects flux calibration errors that are within expectations. Even in these objects, however, the $5.8 \mu\text{m}$ band intensity is 2–3 times stronger than what can be attributed to H_2 ; and in the three other objects, the contribution of H_2 to either the $5.8 \mu\text{m}$ or $8 \mu\text{m}$ band is small, at least averaged over the entire mapped

region. Nevertheless, the IRAC maps shown in Figures 11–15 can exhibit clear morphological similarities to the H_2 line maps, even in objects such as L1448 where the overall contribution of H_2 is small. This reflects the fact that regions of diffuse emission can be H_2 -dominated even if compact continuum sources account for most of the IRAC intensity when averaged over the entire region that we have mapped. Finally, we note that in the case of VLA 1623 and NGC 2071, the contributions listed in Table 3 reflect an important selection effect: we specifically avoided observing H_2 emissions in those regions known to exhibit the strongest continuum emission, because they would have saturated the IRS detectors. Thus, had we been able to map the entire object with IRS, the fractional contributions of H_2 listed in Table 3 would have been even smaller, probably by a large factor. In summary, a comparison of the IRS and IRAC data indicates that the $8 \mu\text{m}$ IRAC channel can be dominated by H_2 emissions for a protostellar outflow, as it was for the SNR IC443 discussed by NY08, but that the H_2 contribution can also be negligible, as in NGC 2071 and VLA 1623.

5. SUMMARY AND FUTURE OUTLOOK

1. We have carried out spectroscopic mapping observations toward protostellar outflows in the BHR71, L1157, L1448, NGC 2071, and VLA 1623 molecular regions using the IRS of the *Spitzer Space Telescope*.

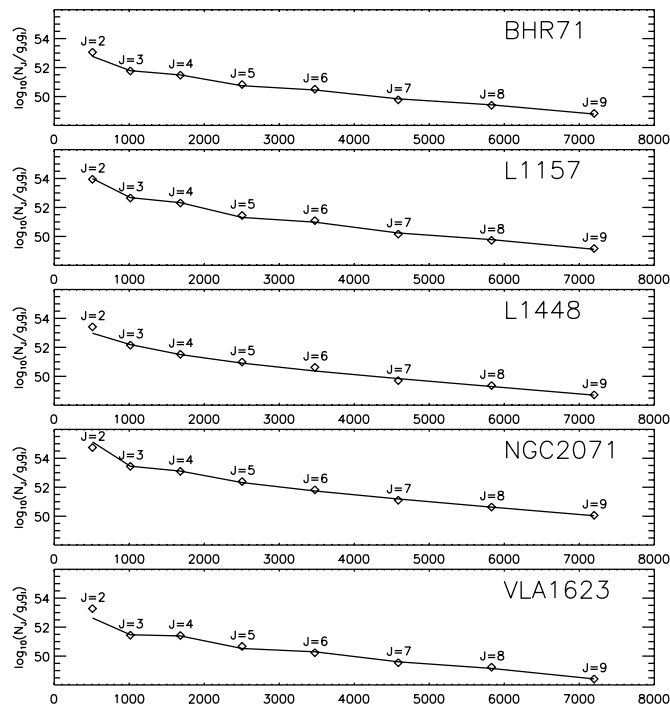


Figure 16. Rotational diagrams for each object. The horizontal axis is the energy of each state, divided by Boltzmann's constant, in units of Kelvin. The vertical axis is the logarithm of the number of molecules in each state, divided by the product of the degeneracies associated with nuclear spin and with rotation. Diamonds indicate the observed values, and the solid lines are results obtained from the fitting procedure described in Section 4.1.

2. Our observations provide detailed maps of the eight lowest pure rotational lines of molecular hydrogen and of the [S I] 25.25 μm and [Fe II] 26.0 μm fine-structure lines.
3. Within the regions mapped toward these five outflow sources, total H_2 luminosities ranging from 0.02 L_\odot to 0.75 L_\odot were inferred for the sum of the eight lowest pure rotational transitions. The overall H_2 luminosities were fitted with a model in which an admixture of gas temperatures is present within the beam. For an assumed power-law distribution of gas temperatures, with the mass of material at temperature T to $T+dT$ assumed proportional to $T^{-b}dT$, the best-fit power-law indices lie in the range 2.3–3.3. With the exception of L1448, all objects exhibit a non-equilibrium H_2 ortho-to-para ratio ≤ 3 . L1157 and NGC 2071 show evidence for an H_2 ortho-to-para ratio that is an increasing function of gas temperature, as expected if para-to-ortho conversion possesses an activation energy barrier.
4. As in SNRs studied by Neufeld et al. (2007), the [S I] 25.3 μm fine-structure emission is more strongly correlated with the H_2 emissions than is the [Fe II] 26.0 μm fine-structure emission. This behavior is consistent with the suggestion that the [Fe II] 26.0 μm fine-structure transition traces faster, dissociative shocks.
5. In BHR71 and L1157, H_2 $S(4)$ and $S(5)$ line emissions account for most of the intensity observed in IRAC 8 μm maps of the region we mapped with IRS.

The primary emphasis in the present paper has been on object-averaged line luminosities. However, the data presented here will allow the construction of line ratio maps that can probe the *variation* of the physical conditions within each

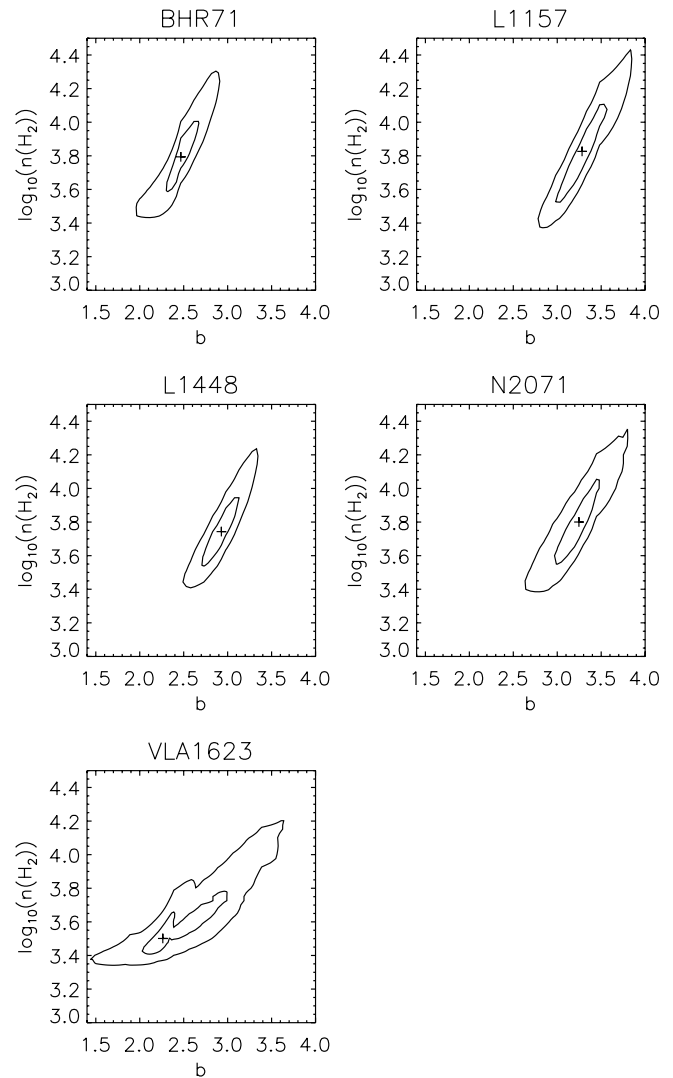


Figure 17. Contours of χ^2 in the b - $n(\text{H}_2)$ plane (see Section 4.1). Crosses indicate the minimum χ^2 (i.e. the best fit), while the two contours represent the 68% and 95% confidence limits on each parameter.

individual object; these will be discussed in a series of future papers.

REFERENCES

- Allen, M. G., Groves, B. A., Dopita, M. A., Sutherland, R. S., & Kewley, L. J. 2008, *ApJS*, **178**, 20
- André, P., Ward-Thompson, D., & Barsony, M. 1993, *ApJ*, **406**, 122
- André, P., Martín-Pintado, J., Despois, D., & Montmerle, T. 1990, *A&A*, **236**, 180
- Bachiller, R., André, P., & Cabrit, S. 1991, *A&A*, **241**, L43
- Bachiller, R., Guilleaume, S., Dutrey, A., Planesas, P., & Martín-Pintado, J. 1995, *A&A*, **299**, 857
- Bachiller, R., Martín-Pintado, J., & Fuente, A. 1991, *A&A*, **243**, L21
- Bachiller, R., Martín-Pintado, J., & Fuente, A. 1993, *ApJ*, **417**, L45
- Bachiller, R., Martín-Pintado, J., Tafalla, M., Cernicharo, J., & Lazareff, B. 1990, *A&A*, **231**, 174
- Bachiller, R., & Perez Gutierrez, M. 1997, *ApJ*, **487**, L93
- Bachiller, R., et al. 2001, *A&A*, **372**, 899
- Bally, J., & Lada, C. J. 1983, *ApJ*, **265**, 824
- Bally, J., Lada, E. A., & Lane, A. P. 1993, *ApJ*, **418**, 322
- Beltrán, M. T., Gueth, F., Guilleaume, S., & Dutrey, A. 2004, *A&A*, **416**, 631
- Bontemps, S., André, P., Terebey, S., & Cabrit, S. 1996, *A&A*, **311**, 858
- Bourke, T. L. 2001, *ApJ*, **554**, L91
- Bourke, T. L., Hyland, A. R., & Robinson, G. 1995a, *MNRAS*, **276**, 1052
- Bourke, T. L., Hyland, A. R., Robinson, G., James, S. D., & Wright, C. M. 1995b, *MNRAS*, **276**, 1067

- Bourke, T. L., et al. 1997, [ApJ](#), **476**, 781
- Caratti o Garatti, A., Giannini, T., Nisini, B., & Lorenzetti, D. 2006, [A&A](#), **449**, 1077
- Chen, X., Launhardt, R., Bourke, T. L., Henning, T., & Barnes, P. J. 2008, [ApJ](#), **683**, 862
- Davis, C. J., & Eislöffel, J. 1995, [A&A](#), **300**, 851
- Davis, C. J., Smith, M. D., Eislöffel, J., & Davies, J. K. 1999, [MNRAS](#), **308**, 539
- Dent, W. R. F., Matthews, H. E., & Walther, D. M. 1995, [MNRAS](#), **277**, 193
- Dionatos, O., Nisini, B., Lopez, R. G., Giannini, T., Davis, C. J., Smith, M. D., Ray, T. P., & DeLuca, M. 2009, [ApJ](#), **692**, 1
- Draine, B. T., & McKee, C. F. 1993, [ARA&A](#), **31**, 373
- Eislöffel, J. 2000, [A&A](#), **354**, 236
- Eislöffel, J., Smith, M. D., & Davis, C. J. 2000, [A&A](#), **359**, 1147
- Enoch, M. L., et al. 2006, [ApJ](#), **638**, 293
- Gómez, M., Stark, D. P., Whitney, B. A., & Churchwell, E. 2003, [AJ](#), **126**, 863
- Grasdalen, G. L., Strom, K. M., & Strom, S. E. 1973, [ApJ](#), **184**, L53
- Gueth, F., Bachiller, R., & Tafalla, M. 2003, [A&A](#), **401**, L5
- Higdon, S. J. U., et al. 2004, [PASP](#), **116**, 975
- Hirano, N., & Taniguchi, Y. 2001, [ApJ](#), **550**, L219
- Jiménez-Serra, I., Martín-Pintado, J., Rodríguez-Franco, A., & Martín, S. 2005, [ApJ](#), **627**, L121
- Jørgensen, J. K., et al. 2006, [ApJ](#), **645**, 1246
- Kaufman, M. J., & Neufeld, D. A. 1996, [ApJ](#), **456**, 611
- Kun, M. 1998, [ApJS](#), **115**, 59
- Loinard, L., Torres, R. M., Mioduszewski, A. J., & Rodríguez, L. F. 2008, in IAU Symp. 248, A Giant Step: from Milli- to Micro-arcsecond Astrometry, ed. W. J. Jin, I. Platais, & M. A. C. Perryman (Dordrecht: Kluwer), 186
- Looney, L. W., Mundy, L. G., & Welch, W. J. 2000, [ApJ](#), **529**, 477
- Looney, L. W., Tobin, J. J., & Kwon, W. 2007, [ApJ](#), **670**, L131
- Loren, R. B., Wootten, A., & Wilking, B. A. 1990, [ApJ](#), **365**, 269
- Maret, S., et al. 2009, [ApJ](#), **698**, 1244
- Melnick, G. J., Tolls, V., Neufeld, D. A., Yuan, Y., Sonnentrucker, P., Watson, D. M., Bergin, E. A., & Kaufman, M. J. 2008, [ApJ](#), **683**, 876
- Mikami, H., Tomofumi, U., Yamamoto, S., & Saito, S. 1992, [ApJ](#), **392**, L87
- Montmerle, T., & André, P. 1988, in NATO ASIC Proc. 241, Formation and Evolution of Low Mass Stars, ed. A. K. Dupree & M. T. V. T. Lago (Dordrecht: Kluwer), 225
- Neufeld, D. A., Hollenbach, D. J., Kaufman, M. J., Snell, R. L., Melnick, G. J., Bergin, E. A., & Sonnentrucker, P. 2007, [ApJ](#), **664**, 890 (N07)
- Neufeld, D. A., & Yuan, Y. 2008, [ApJ](#), **678**, 974 (NY08)
- Neufeld, D. A., et al. 2006, [ApJ](#), **649**, 816 (N06)
- Nisini, B., Benedettini, M., Giannini, T., Codella, C., Lorenzetti, D., di Giorgio, A. M., & Richer, J. S. 2000, [A&A](#), **360**, 297
- Nisini, B., Codella, C., Giannini, T., Santiago Garcia, J., Richer, J. S., Bachiller, R., & Tafalla, M. 2007, [A&A](#), **462**, 163
- Nisini, B., et al. 1999, [A&A](#), **350**, 529
- Parise, B., et al. 2006, [A&A](#), **454**, L79
- Reach, W. T., et al. 2006, [AJ](#), **131**, 1479
- Sandqvist, A. 1977, [A&A](#), **57**, 467
- Schofield, K. 1967, [Planet. Space Sci.](#), **15**, 643
- Schulz, W. R., & Le Roy, D. J. 1965, [J. Chem. Phys.](#), **42**, 3869
- Sonnentrucker, P., González-Alfonso, E., & Neufeld, D. A. 2007, [ApJ](#), **671**, L37
- Sonnentrucker, P., González-Alfonso, E., Neufeld, D. A., Bergin, E. A., Melnick, G. J., Forrest, W. J., Pipher, J. L., & Watson, D. M. 2006, [ApJ](#), **650**, L71
- Viotti, N. R. 1969, [Mem. Soc. Astron. Ital.](#), **40**, 75
- Wolf-Chase, G. A., Barsony, M., & O’Linger, J. 2000, [AJ](#), **120**, 1467